Precipitating electron energy spectra and auroral power estimation by incoherent scatter radar with high temporal resolution

Habtamu W. Tesfaw [1], Ilkka I. Virtanen[1], Anita Aikio[1], Amoré Nel[2], Michael Kosch[2,3,4], and Yasunobu Ogawa[5]

[1]Space Physics and Astronomy Research Unit, University of Oulu, Oulu, Finland
[2]South African National Space Agency, Hermanus, South Africa
[3]Physics Dept., Lancaster University, Lancaster, UK
[4]Dept. of Physics and Astrophysics, University of Western Cape, Bellville, South Africa.
[5]National Institue of Polar Research, Tokyo, Japan

Key Points:

- We use the BAFIM-ELSPEC analysis combination to calculate the energy spectra of precipitating electrons with high time resolution (4 s).
- Using the true electron density data in precipitation events leads to wider energy spectra, and larger auroral power and FAC estimates.
- Auroral power calculated using the BAFIM-ELSPEC analysis agrees very well with that of the 427.8 nm emission line intensity.

Corresponding author: Habtamu W. Tesfaw, Habtamu.Tesfaw@oulu.fi

Abstract

High-resolution incoherent scatter radar (ISR) observations of the E region electron density are customarily based on raw electron density, because accuracy of the high-resolution incoherent scatter spectra are typically insufficient for a full fit of plasma parameters using existing data analysis tools. Raw densities have also been used for electron precipitation energy spectrum inversion from ISR data. In this study, we use the Bayesian Filtering Module (BAFIM) to fit the true E region electron density, electron and ion temperatures, and ion velocity to ISR data with high resolutions in time and range, 4 s and 1.8 km correspondingly. We use the EISCAT UHF radar observation of an auroral event on March 09, 2016 over Tromsø. Both the raw electron density and the true one are then inverted into electron energy spectra using the ELSPEC software. Usage of true electron densities leads to wider electron energy spectra, auroral power up to 75% larger and upward field-aligned current up to 90% larger than usage of raw electron densities. The largest differences take place for precipitation activities which produce enhanced electron heating in the upper E region and in this study correspond to flux of electrons with peak energies from 3 to 5 keV. Finally, we compare the auroral power estimates calculated using BAFIM-ELSPEC analysis to the 427.8 nm auroral emission intensity (proportional to the total energy flux) and find a good agreement.

1 Introduction

Night time ionization enhancements in the high-latitude E region ionosphere are caused by electron precipitation through impact ionization of neutral atoms and molecules. An optical signature of the electron precipitation are auroral emissions, which are produced when excited atoms, molecules, and ions return to their ground states. Electron precipitation is quantitatively characterized by the energy distribution of the primary electrons. Electron acceleration processes in the magnetosphere that lead to different energy spectral shapes are discussed by Newell et al. (2009) and Dombeck et al. (2018). For a known differential energy flux, altitude profiles of ion production rate and auroral emission rates can be determined if the neutral atmospheric parameters are known (Rees, 1963; Fang et al., 2010).

Indirect estimation of the differential energy flux from electron density altitude profiles observed with an incoherent scatter radar (ISR) is an efficient way to observe electron precipitation from ground (Vondrak & Baron, 1977; Kirkwood, 1988; Brekke et al., 1989; Semeter & Kamalabadi, 2005; Kaeppler et al., 2015; Simon Wedlund et al., 2013; Virtanen et al., 2018). Unlike in situ observations with fast moving satellites and rockets, the radar observations allow one to follow the time evolution of the electron precipitation along the local geomagnetic field.

Two different analysis techniques are commonly used to obtain electron densities from an ISR observation. Scaling the backscattered power with radar system parameters results in the so-called raw electron density (N_r), which is equal to the actual electron density (N_e) if electron and ion temperatures are equal. A more sophisticated way is to make a least-squares fit of a parametric incoherent scatter spectrum model to the observed spectra. Typically, electron density (N_e), electron temperature (T_e), ion temperature (T_i), and line-of-sight ion bulk velocity (V_i) are fitted.

The electron density profiles need to be observed with high resolutions in range and time to enable accurate estimation of the rapidly varying electron energy spectra. While plasma parameter fits to EISCAT ISR data are typically made with a few kilometer range resolution and some tens of seconds time resolution using the Grand Unified Incoherent Scatter Design and Analysis Package (GUISDAP) (Lehtinen & Huuskonen, 1996), the electron energy spectra fits require range resolution better than 2 km (Semeter & Kamalabadi, 2005) and time resolution of the order of five seconds (Virtanen et al., 2018).

Since other high-latitude ISR facilities cannot produce better resolutions either, previous high time resolution energy spectrum fits have been based on raw electron densities (Burns et al., 1990; Lanchester et al., 1994, 1996, 1997; Semeter & Kamalabadi, 2005; Dahlgren et al., 2011; Virtanen et al., 2018), while the fitted electron densities have been used with 1 min or coarser resolutions (Hargreaves & Devlin, 1990; Kirkwood & Eliasson, 1990; Strickland et al., 1994; Fujii et al., 1995; Osepian & Kirkwood, 1996; Kosch et al., 2001; Kaeppler et al., 2015). However, the electron precipitation tends to heat the electron gas, which makes the implicit assumption of $T_e = T_i$ questionable in calculation of N_r. The raw density N_r is smaller than the actual density N_e if $T_e > T_i$, which may lead to underestimation of the precipitating energy flux if N_r is used in electron energy spectrum fits.

The aim of this study is to perform full four-parameter fits to the observed incoherent scatter spectra with 4 s time resolution and 1.8 km range resolution and to use the actual fitted N_e in high-resolution electron energy spectrum fits for the first time. The high-resolution plasma parameter fit is possible with the newly developed Bayesian Filtering Module (BAFIM) (Virtanen et al., 2021), and electron energy spectra are fitted to the observed electron density profiles using the ELSPEC software (Virtanen et al., 2018). The BAFIM-ELSPEC analysis combination will be applied to an auroral event that comprises wide range of auroral features. By comparing the ELSPEC analysis results obtained from the fitted and raw electron densities, we will study effects of enhanced electron heating on the calculated energy spectra of the precipitating electrons.

To validate our auroral power estimates, we will compare the auroral power (total energy flux) calculated from BAFIM-ELSPEC analysis combination with that of the 427.8 nm spectral (blue) line emission intensity of the N_2^+ molecular ions. Previous studies have shown direct proportionality between line of sight integrated blue line emission intensity and total energy flux of the precipitating electrons (Omholt, 1971; Rees & Luckey, 1974; Strickland et al., 1989; Partamies et al., 2004). Recently, Kaeppler et al. (2015) have made such comparisons in which the energy flux is calculated from a fitted electron density data with 4.5 km range, and 1 and 3 min time resolutions which are much coarser than our ISR data analysis results. Their focus was on stable auroral features.

The paper is organized as follows; data and measurements are introduced in Section 2, the auroral event is described in Section 3, the radar data analysis and the effect of electron heating are discussed in Section 4, and auroral power derived from the radar observations is compared to optical observations in Section 5. Discussion and summary are presented in Section 6.

2 Data and Measurements

The active auroral event presented in this study took place on 9 March 2016, 19:40 - 23:40 UT over Tromsø, Norway. The EISCAT UHF radar near Tromsø (69.58°N, 19.23°E Geodetic, and 66.67°N, 101.41°E Geomagnetic) was pointed along the local geomagnetic field and it was running the 'arc1' experiment, which uses a 64-bit alternating code sequence (Lehtinen & Häggström, 1987) with 6 μs bit length. The 128 pulses of the code sequence were transmitted with 3.468 ms inter-pulse periods, and autocorrelation function data decoded to 900 m range resolution were stored from each 443.9 ms long pulse sequence. In this study we use data integrated to 4 s time resolution.

In addition to the ISR observations, we characterize the dynamics of the observed auroral structures using all-sky camera (ASC) and narrow field of view optical observations. All-sky images of the auroral green line emission (557.7 nm) with 1 s time resolution are obtained from the Watec monochromatic imager (WMI) (Ogawa et al., 2020) located at the EISCAT Tromsø radar site. In addition, we use an EMCCD imager located at the radar site (Nel et al., 2021) for narrow field of view (FoV) observations of

small-scale auroral structures around and within the radar beam. The detector images auroral emissions at wavelength 427.8 nm from relaxation of the N_2^+ molecules with a 30° FoV and 3 s exposure time. The camera system was pointing to the geomagnetic zenith.

Local and global auroral electrojet indices are also used to monitor the geomagnetic activity. Geomagnetic field data obtained from the IMAGE network of magnetometers are used to derive local auroral electrojet indices IL (Kallio et al., 2000). Finally, an induction coil magnetometer at Kilpisjärvi (69.06°N, 20.77°E Geodetic, and 66.07°N, 102.30°E Geomagnetic) is used to monitor the geomagnetic pulsation activity.

3 Event Description

Overview of the event is given in Figure 1. A time lapse video of the ASC and narrow FoV auroral images is provided as a supplementary material. The raw electron density obtained from the EISCAT UHF radar observation is placed in the first panel of the figure. Keograms produced from the North-South cut of the narrow FoV and ASC auroral images over the radar zenith are shown in the second and third panels, respectively. We make coordinate transformation at 110 km to calculate the latitudes for the keograms. The horizontal white lines in the keograms represent position of the radar beam. Power spectra of geomagnetic pulsations, and local (IL) and global (AL) auroral electrojet indices are shown in the fourth and fifth panels, respectively. Selected all-sky auroral images are shown in Figure 2. Magnetic midnight at Tromsø is at about 21:30 UT.

At 19:30 UT there were several faint arcs in the FoV of the ASC which later drifted equatorward. After few minutes, at about 19:39 UT, the first signature of an intensification of an arc is seen in the eastern horizon. At about the same time, the peak frequency in the pulsation power spectrum jumps from below 1 mHz to about 0.5 Hz, which indicates development of PiB pulsations (McPherron, 2005; Olson, 1999). PiB pulsation development and sudden brightening of auroral arcs are typical indicators of substorm activation (Sakurai & Saito, 1976; Mishin et al., 2020). The IL and AL indices decrease abruptly at about 19:40, which is another indication of substorm onset (Tanskanen, 2009; Hsu & McPherron, 2012).

Based on the AL index, three relatively small substorm onsets took place during the studied time interval with rough onset times at 19:40, 21:30 and 22:40 UT. During the first substorm, the IL index remained much smaller than the AL index indicating that the substorm onset region was not in Scandinavia, but rather to the east, closer to magnetic midnight.

In addition to the continuous PiB activity, magnetic pulsations show signatures of Pc1 pulsations near 1 Hz, which are produced by protons injected to the inner magnetosphere and interacting with ion cyclotron waves (Saito, 1969). It is probable that this injection is a consequence of substorm onset.

The radar starts recording large ionization enhancements after 19:44 UT when the most equatorward arc, which was within the radar beam, became bright. This wide bright auroral arc stays within the beam until 19:51 UT, as shown in auroral images A and B of Figure 2, and produces the first period of enhanced ionization between 19:44 and 19:51 UT. The arc then fades in its intensity, and by 19:52 UT it is substituted by several east-west aligned arcs forming together a bright bulge that expands poleward. Selected images of the bulge are shown in panels C and D of Figure 2.

Probing the poleward advancing bulge, the radar measures an ionization enhancement between 19:52 and 20:00 UT. The bulge leaves the radar beam at about 20:01 UT and continues expanding poleward until 20:04 UT. Then it starts to retreat from its poleward extent and advances equatorward across the radar beam. As indicated in auroral

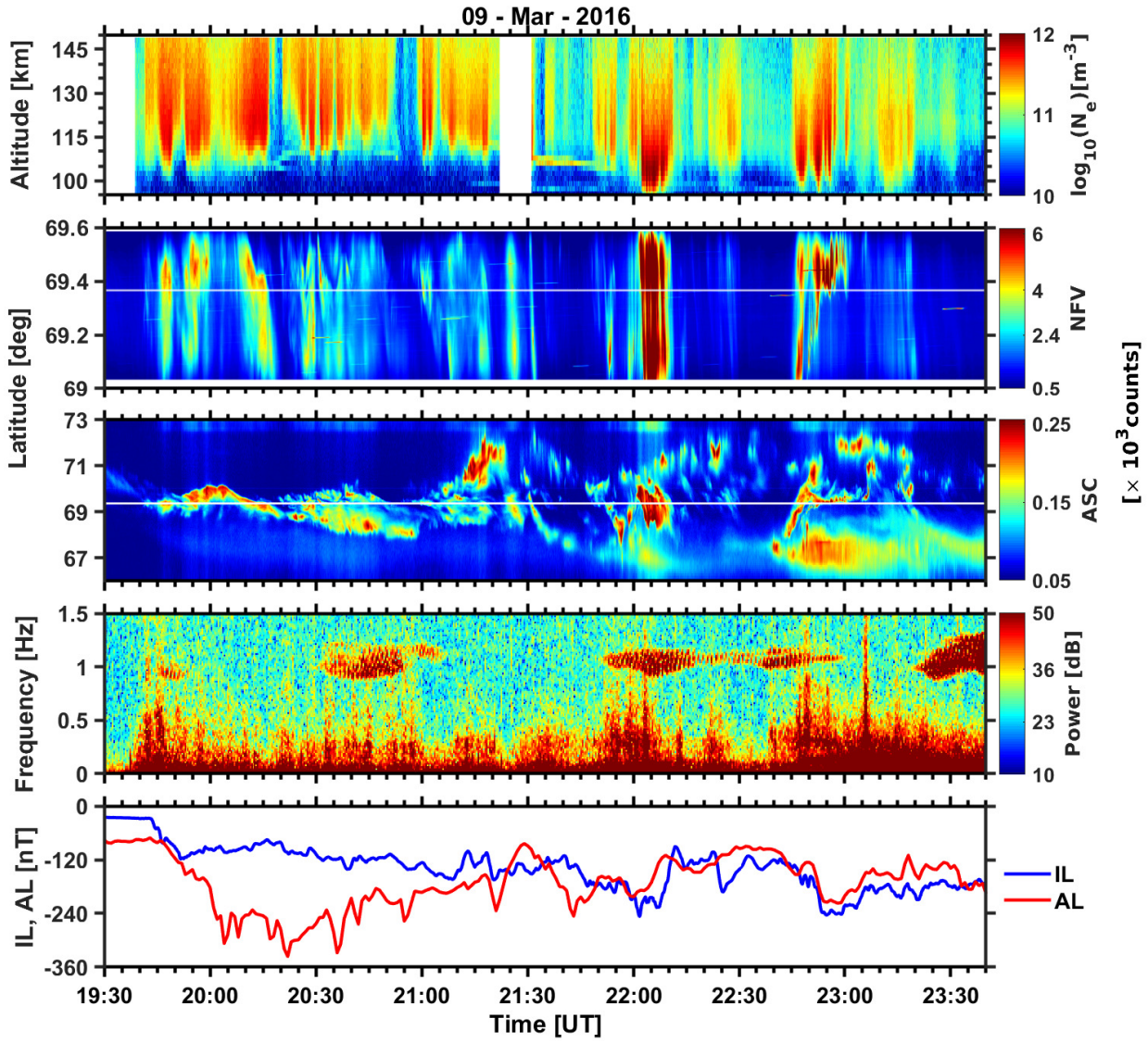

Figure 1. An overview of the auroral event. Panels from top to bottom: raw electron density, narrow FoV keogram (427.8 nm), ASC Keogram (557.7 nm), geomagnetic pulsation spectrogram, and IL and AL electrojet indices.

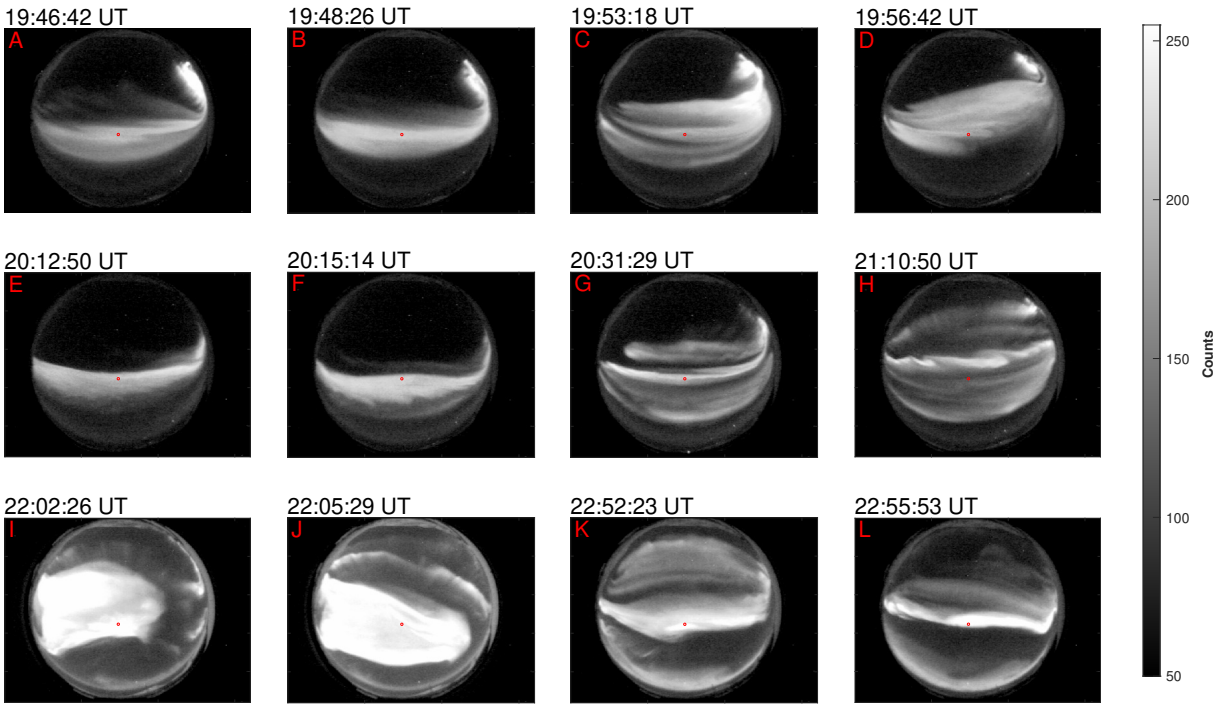

Figure 2. Selected auroral images taken from the ASC camera observation on 9 March, 2016. The radar beam is shown as a red dot in the images. North is up and east is to the right.

images E and F of Figure 2, the radar was observing the equatorward moving arc between 20:07 and 20:16 UT to produce the third ionization enhancement. The east-west aligned arc continued drifting equatorward and left the radar beam at about 20:16:30 UT.

At about 20:22 UT, the AL index attained its minimum value of about -350 nT, indicating the end of the first substorm expansion phase. During the first substorm recovery phase, between 20:20 and 21:30, multiple auroral features with folds and curls are created across the auroral oval as shown in the ASC and narrow FoV keograms in Figure 1. Sample auroral images taken from this time interval are shown in panels G and H of Figure 2. When these auroral structures perform radar beam crossings, series of several short lived ionization enhancements are produced between 20:20 and 21:20 UT.

During the first substorm, all the arcs were streaming mostly towards the west. Counter-streaming arcs were also observed so that in the northern part the streaming was to the east and in the southern part towards the west, indicating converging electric field structure and auroral potential drop above the the ionosphere (Carlson et al., 1998; Aikio et al., 2002). Spectra of the electron flux corresponding to the arcs will also show inverted-V type structures, as we will see later.

Following break up of the second substorm at about 21:30 UT, a bright auroral feature is seen in the north-west horizon of the ASC at about 21:35 UT, indicating the onset region of this substorm was to the west of Tromsø. After the onset, the streaming inside the arcs becomes mainly eastward. Eventually a bright auroral bulge, expanding to the ASC FoV from the west, is formed at about 21:57 UT. Selected images of the bulge are shown in panels I and J of Figure 2. When the bulge passes through the radar beam at about 21:59, it produces an electron density enhancement characterized by largest peak

electron densities (in the order of 10^{12} m^{-3}) and lowest peak altitudes (about 100 km) of the event. The narrow FoV and ASC keograms show that the radar beam was at the center of this intensifying bulge from 22:00 until 22:11 UT. The auroral bulge fades in its intensity by 22:12. After that and until 22:40 several auroral features with varying luminosity are observed across the horizon of the ASC.

The AL index shows that onset of the third substorm occurs at about 22:40 UT. Indeed, at 22:39 UT an auroral arc was observed intensifying from west to east in the very southern horizon of the ASC, indicating the onset was to the west of Scandinavia. Auroral images K and L of Figure 2 show that the radar measured the last ionization enhancement between 22:44 and 22:56 UT when these auroral arcs drift poleward. ASC and narrow FoV keograms indicate that the radar was observing the equatorward edge of an east west aligned auroral arc between 22:53 and 22:56 UT.

In addition to ionization by precipitating electrons, sporadic E layers can be seen during two time intervals in the electron density plot. The first sporadic E layer is observed between 20:20 and 20:52 UT, and the second one is between 21:30 and 21:48 UT.

4 Electron Energy Spectrum Analysis

The analysis method we use to calculate the differential electron energy flux from the EISCAT UHF ISR data consist of two steps. First, plasma parameters are fitted to the incoherent scatter data with 4 s time resolution and 1.8 km range resolution using the combination of GUISDAP (Lehtinen & Huuskonen, 1996) and BAFIM (Virtanen et al., 2021). Second, the fitted electron density altitude profiles are inverted into differential energy fluxes of precipitating electrons using the ELSPEC software (Virtanen et al., 2018). In this section, we introduce the analysis methods and address the effect of electron heating on the raw electron density N_r for the first substorm discussed in Section 3. We consider both the bias in raw electron density and its effects on the electron energy spectrum fits.

4.1 Fitted and raw electron densities

In the traditional 'gated' incoherent scatter plasma parameter fits, one averages the incoherent scatter autocorrelation function (ACF) over selected intervals in range and time, and fits the plasma parameters to the averaged autocorrelation functions in each range-gate and time-step. Each fit is independent of the others and one cannot include prior information about shape of the plasma parameter profiles, or about their expected temporal variations. Statistical accuracy of the fitted plasma parameters depends on the resolutions, since accuracy of the observed ACF is improved with increasing integration in time or range. The standard GUISDAP analysis of EISCAT radar data uses the gated analysis principle. Accuracy of the GUISDAP fit results depends also on the level of ionization in the observed region, which affects the signal-to-noise ratio. Although E region electron density is typically high during active aurora, resolutions needed to follow the associated rapid variations in electron energy spectra are practically out of reach of the standard four-parameter fits of N_e, T_e, T_i, and V_i with GUISDAP.

Due to the limitations of the four-parameter fits, the high-resolution electron density observations are typically based on the raw electron density, which is the backscattered signal power multiplied with radar system parameters. Assuming that the Debye length is much smaller than the radar wavelength, which is a well justified assumption in E region observations with the EISCAT UHF radar, the relation between the raw density N_r and the actual density N_e can be written as (Baron, 1977; Semeter & Kamalabadi, 2005),

$$N_r = \frac{2N_e}{(1 + T_r)}, \tag{1}$$

where $T_r = T_e/T_i$. Obviously, $N_e = N_r$ when $T_r = 1$, but $N_e > N_r$ when $T_r > 1$. For example, $N_e = 1.5 \cdot N_r$ if $T_r = 2$, which is not an unusual temperature ratio in the upper E region during electron precipitation. Auroral events with enhanced E region electron temperature have been investigated e.g. by Wickwar et al. (1981), who found that the electron density altitude profiles calculated with correct temperature ratio have lower peak altitudes and greater peak electron densities than those of the raw electron density altitude profiles.

An alternative to the gated analysis is the full-profile analysis (Holt et al., 1992; Lehtinen et al., 1996; Hysell et al., 2008), in which one fits full range-profiles of plasma parameters. The full-profile analysis allows one to include prior information about the plasma parameter profiles, but it is also computationally heavier than the gated analysis. The Bayesian Filtering Module (BAFIM) (Virtanen et al., 2021) is an extension module to GUISDAP, which allows one to include prior information about plasma parameter gradients in both range and time in gated GUISDAP analysis. BAFIM thus extends the idea of full profile analysis to smoothness in both range and time, but without increasing the computational burden of the gated analysis. BAFIM introduces correlations in between adjacent range-gates and time-steps in a way that leads to effectively coarser resolutions in range and time than those defined by the range-gates and time-steps. Since the correlations are defined for each plasma parameter separately, one can use effectively coarser resolutions for T_e, T_i, and V_i, but fit the electron density N_e with the best possible resolution. The assumption of smoothness in the T_e and T_i profiles is justified in field-aligned observations, because the high mobility along the magnetic field prevents generation of large field-aligned temperature gradients in the upper E and lower F regions.

4.2 High resolution plasma parameter fit with BAFIM

For this study, we ran a BAFIM fit of N_e, T_e, T_i, and V_i on the EISCAT UHF radar data with 1.8 km range steps and 4 s time steps. BAFIM was tuned so that the "effective" time and range resolutions of N_e are very close to the time and range steps, while resolutions of the other plasma parameters are effectively coarser. Interested readers are referred to Table 1 of Virtanen et al. (2021) for the values of the tuned analysis parameters and their physical meanings. For this particular study, however, we changed the electron density correlation length $\left(s^h\right)$ and process noise $\left(s^t\right)$ scaling parameters to 0.1 and $1.0{\cdot}10^{12}$ $\mathrm{m}^{-3}\mathrm{s}^{-1/2}$, respectively. The 1.8 km resolution was chosen, because it produces better temperature estimates than the 0.9 km resolution, and the change from 0.9 km to 1.8 km resolution did not affect results of the subsequent ELSPEC analysis. The raw electron density is first calculated from the same data with 0.9 km range resolution and 4 s time resolution, and then integrated in range to 1.8 km range resolution to match the corresponding resolution of the BAFIM analysis. The alternating code experiment does not provide true backscattered powers, but the raw density is calculated from a short non-zero lag of the autocorrelation function.

In order to demonstrate the bias in the raw electron density and its subsequent effect on the energy spectra analysis, we choose for the analysis expansion phase of the first substorm during which pronounced electron heating was observed. The electron density (N_e) and temperature ratio (T_e/T_i) fit results obtained from the BAFIM analysis are placed in the first and fourth panels of Figure 3, respectively. The raw electron density (N_r) is shown in second panel of the figure. The difference $N_e - N_r$ is shown in the third panel. As shown in the first and second panels of Figure 3, three intervals of enhanced ionization can be identified from the electron density plots, which are associated to specific auroral features discussed in Section 3.

As shown by the bottom panel of the figure, time intervals with $T_r > 1$ match with the periods of enhanced ionization. These concurrent enhancements indicate that the

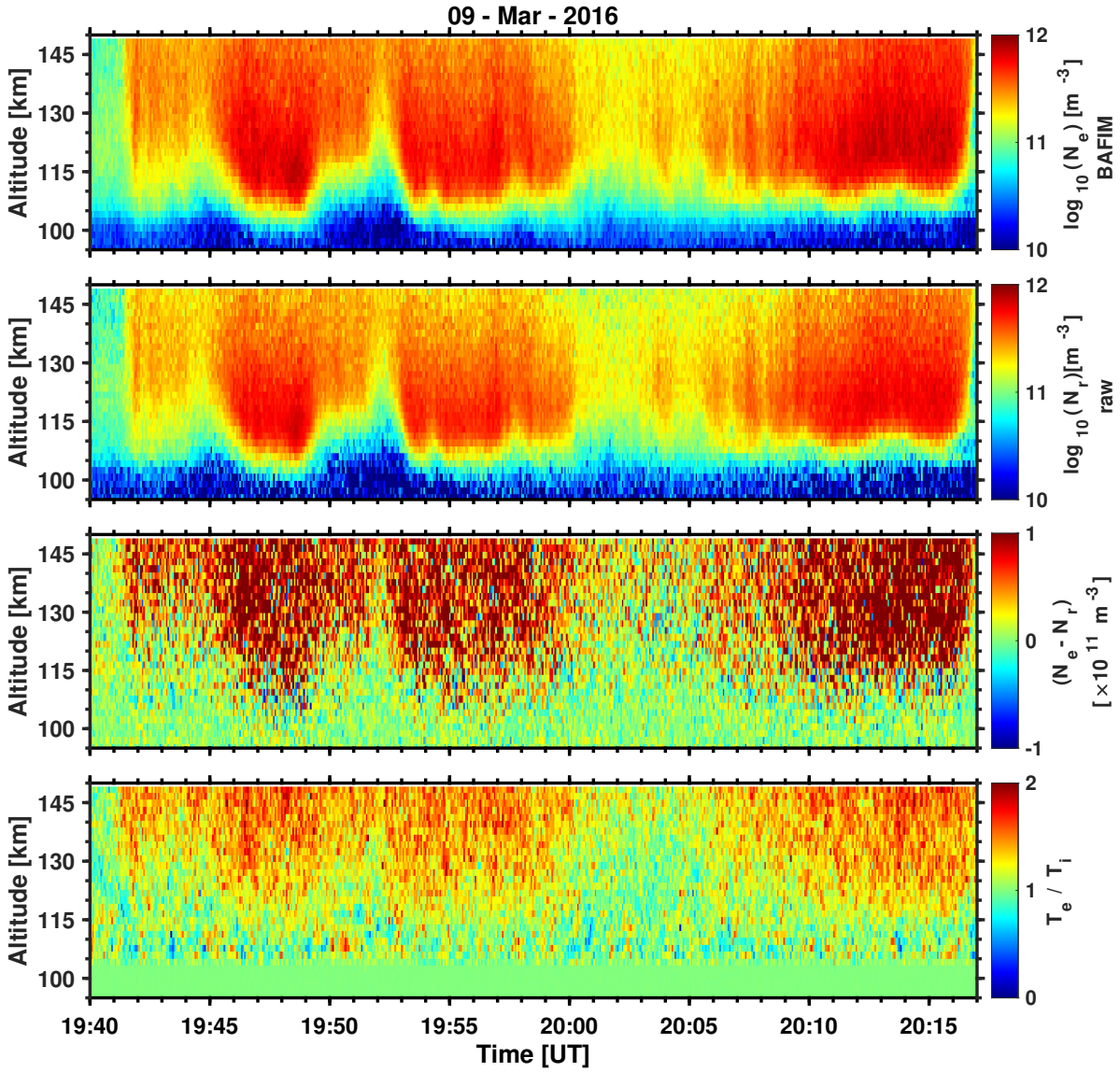

Figure 3. Comparison of the raw electron density N_r and the BAFIM-fitted density N_e. Panels from top to bottom: BAFIM N_e, raw density N_r, Difference $N_e - N_r$, and temperature ratio T_e/T_i from the BAFIM fit.

energy deposited during the course of precipitation is the cause of the observed electron gas heating. A well established elevation in the electron temperature ($T_r > 1$) can be identified, on average, above about 115 km during all periods of enhanced ionization. In addition, T_r is shown to increase substantially with altitude to values greater than 1.5 above 130 km during each period of enhanced ionization. Below 103 km we do not fit the temperature ratio, rather we assume $T_r = 1$, which is a valid assumption since collision balances the ion and electron temperatures at these altitudes.

The third panel of Figure 3 shows significant differences between the BAFIM electron density and raw electron density estimates during times of electron heating, i.e. when $T_r > 1$. Substantial difference (of the order of 10^{11} m^{-3}) can be identified down to 115 km altitude during each period of enhanced ionization. The observed differences increase substantially with altitude and reach about 50% close to 150 km altitude. On the other hand, although the ionization enhancements extend down to 100 km altitude, the difference between BAFIM-fitted and raw electron densities is insignificant below 115 km. This is because frequent collisions balance the electron, ion, and neutral temperatures at these altitudes.

4.3 Electron energy spectrum fit with ELSPEC

We use the ELSPEC software (Virtanen et al., 2018) to invert the electron density altitude profiles into differential number flux of the precipitating electrons. ELSPEC solves the electron continuity equation that involves the ion production (Q) and loss $\left(L = \alpha N_e^2\right)$ rates,

$$\frac{dN_e}{dt} = Q - \alpha N_e^2. \tag{2}$$

The ion production rate Q as function of differential electron number flux is calculated using the model of Fang et al. (2010). The effective recombination coefficient α is a function of ion composition and electron temperature (Sheehan & St.-Maurice, 2004). ELSPEC assumes constant electron flux and recombination coefficient during a radar integration time (4 s in our case), and integrates the modeled electron density as function of time from the continuity equation. The differential electron number flux is then solved by means of minimizing the difference of the modeled density profile averaged over a radar integration, and the observed electron density profile. The technique is targeted for auroral electrons with energies between 1 and 100 keV, which ionize the atmosphere between 80 and 150 km altitudes.

Originally, ELSPEC used raw electron densities (N_r) as input to high resolution analysis, because the four-parameter fits were not possible with high resolutions. The electron temperature data needed for the recombination speed calculations was taken from standard GUISDAP fits with 60 s time and a few km range resolutions, and interpolated to the time and range resolutions of the raw electron density. In this study, we use the BAFIM-fitted high-resolution (4 s/1.8 km) N_e and T_e as inputs to ELSPEC for the first time. In order to study how much the fitted energy spectra change when the raw electron density N_r is replaced with the fitted N_e, we ran the ELSPEC analysis also with the raw density N_r as input.

4.4 Effect of electron heating on energy spectrum fit

We applied the ELSPEC analysis on the raw and BAFIM-fitted electron densities shown in Figure 3 to demonstrate the effect of electron heating on the electron energy spectra fits. This time interval corresponds to the expansion phase of the first substorm during which enhanced electron gas heating was observed for several minutes. Figure 4 shows comparison of ELSPEC fit result with raw density N_r and fitted density N_e as inputs. From top to bottom, the panels are the BAFIM-fitted electron density (N_e), the differential energy flux inverted from the BAFIM N_e (I_b), the differential energy flux in-

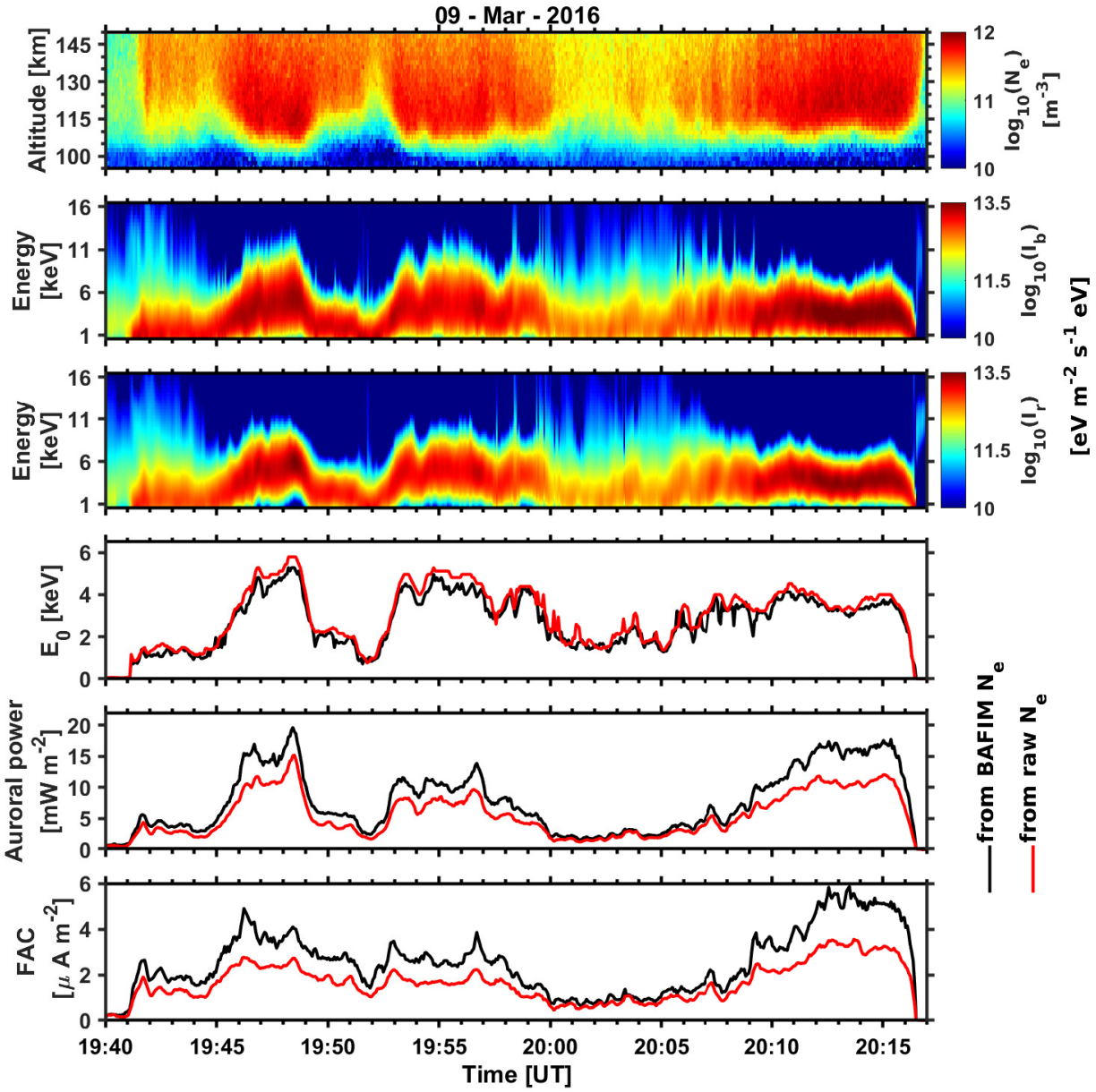

Figure 4. Comparison of ELSPEC fit results using raw density N_r and the BAFIM-fitted density N_e as inputs. Panels from top to bottom: The BAFIM-fitted N_e, the differential electron energy fluxes inverted from the BAFIM-fitted N_e (I_b) and raw density (I_r), peak energies (E_0), auroral powers, and field-aligned currents (FAC). In panels 4-6, the black and red curves correspond to the BAFIM-fitted and raw electron density results, respectively.

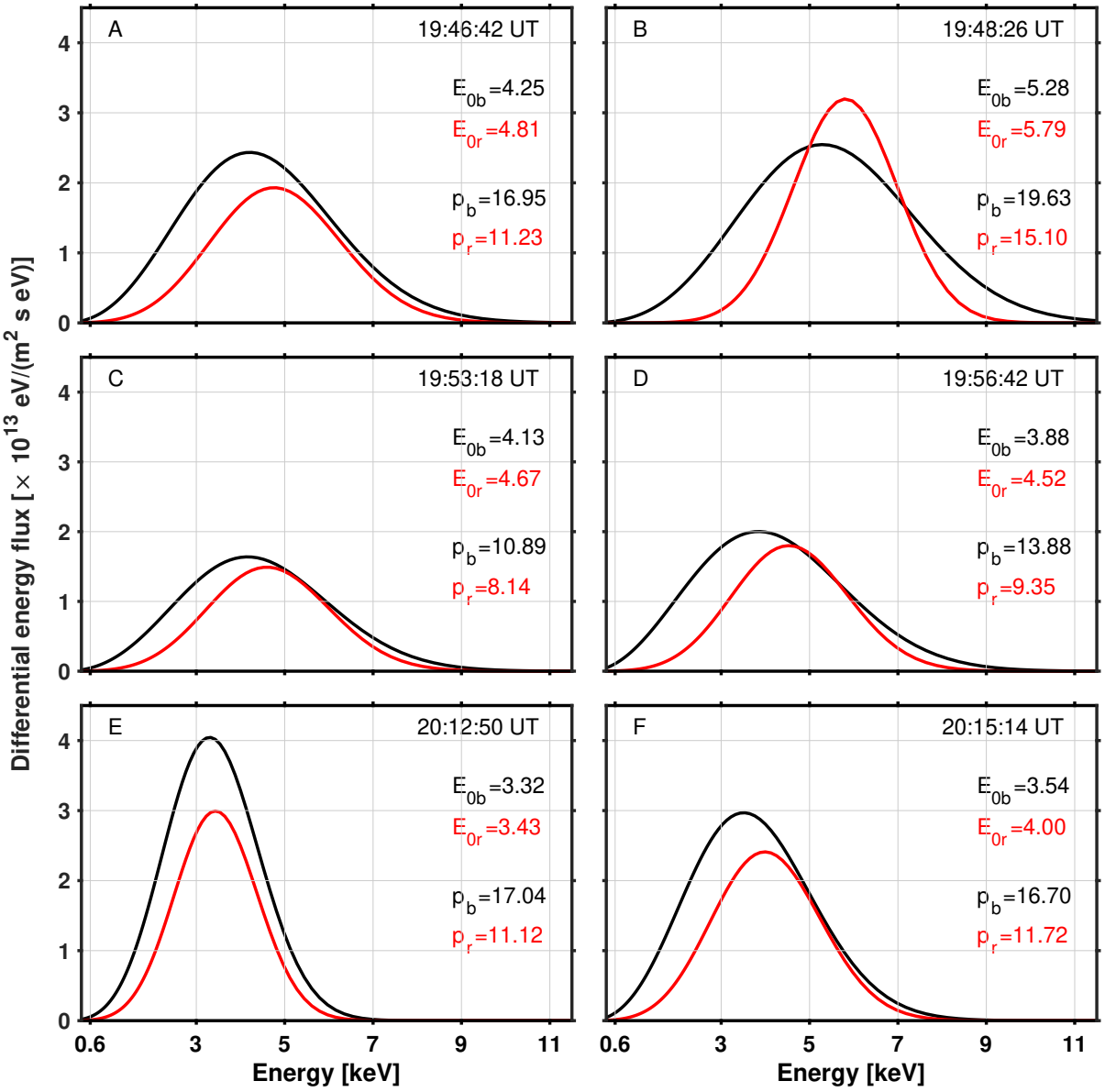

Figure 5. Comparison of selected differential energy flux estimates calculated from BAFIM-fitted electron density N_e (black) and raw electron density N_r (red). E_{0b} and P_b are the peak energies (in keV) and auroral power estimates (in mWm^{-2}) calculated from the BAFIM-fitted N_e. E_{0r} and P_r are the corresponding quantities calculated from the raw density N_r.

verted from the raw density N_r (I_r), peak energy (E_0), auroral power, and field aligned current (FAC). The peak energy is the energy at which the differential energy flux reaches its maximum value. The auroral power, which is equal to the total energy flux, is calculated by integrating the differential energy flux over all energies above 1 keV. The field aligned current is proportional to the total number flux, which is calculated by integrating the differential number flux. The FAC estimate represents the upward electric current carried by the downward precipitating electrons.

Comparing the second and third panels of Figure 4, wider energy distribution is observed in the energy spectra calculated from BAFIM N_e than in the one obtained from raw density N_r. Specifically, larger flux is observed in the lower energy ends of I_b than in that of I_r. On the other hand, the peak energy obtained from raw density N_r slightly exceeds the one obtained from BAFIM N_e (4^{th} panel). This is another indication that the energy distribution obtained from BAFIM N_e tends to have a larger electron flux at its lower energy ends. The larger flux at lower energy ends of I_b account for $N_e > N_r$ above 115 km altitude, as discussed in Subsection 4.2.

The 5^{th} panel of Figure 4 shows a pronounced difference between the auroral power estimates during the first and last periods of enhanced ionization. In the first time period, between 19:45 and 19:48 UT, a difference of 5 mWm^{-2} is observed, whereas in the last time period, between 20:09 and 20:16 UT, the difference is about 6 mWm^{-2}. During both periods, the auroral power calculated from the BAFIM-fitted N_e exceeds its counterpart calculated from raw density N_r by about 50%. The 6^{th} panel of Figure 3 shows a significant difference between the FAC estimates for a longer period of time, between 19:45 and 19:57 UT. Within the given time interval, the difference between the FAC estimates is about 2 $\mu\mathrm{Am}^{-2}$ (70%). Between 20:09 and 20:15 a 2.6 $\mu\mathrm{Am}^{-2}$ (65%) difference is observed. In general the total energy flux and number flux estimates obtained from BAFIM N_e exceed those obtained from raw density N_r during each period of enhanced ionization. Detailed distribution of the differences in auroral power and FAC estimates across the entire data will be discussed in Subsection 4.5.

Figure 5 shows line plots of selected differential energy flux estimates derived from the BAFIM-fitted N_e (black) and raw density N_r (red). The line plots in panels A -F of the figure show energy spectra of the precipitating electrons that produce the corresponding auroral arcs shown in panels A - F of Figure 2. The peak energies (in keV) and auroral power estimates (in mWm^{-2}) at the given time instants are also shown in the figure. All the line plots distinctly demonstrate that the differential energy flux calculated from the BAFIM-fitted N_e contains larger energy flux below its peak energy than its counterpart calculated from the raw electron density. In addition, the energy spectra obtained from the raw electron density N_r shows narrower energy distribution as compared to its counterpart calculated from the BAFIM-fitted N_e.

Inferring the BAFIM-ELSPEC analysis results in the figure, the bright arcs inside the radar beam shown in Figure 2 are produced by precipitating electrons of peak energies between 3 and 5 keV. In addition, the total energy flux of the electrons that powers the arcs lies in the range between 10 and 20 mWm^{-2}. The 20 mWm^{-2} auroral power, the largest one here, corresponds to the bright auroral arc observed in the early expansion phase of the first substorm, at about 19:48 UT, as shown in Figure 2.

4.5 Electron energy spectra from the whole time interval

Figure 6 shows different parameters derived from the radar data of the entire event that comprises the three substorm activities. In the first and second panels, we have the BAFIM-fitted N_e and the corresponding differential energy flux results, respectively. The peak energy, auroral power and FAC estimates are placed in the remaining panels from top to bottom. In panels 3-4, the black and red curves represent parameters derived from the BAFIM-fitted and raw electron density results, respectively.

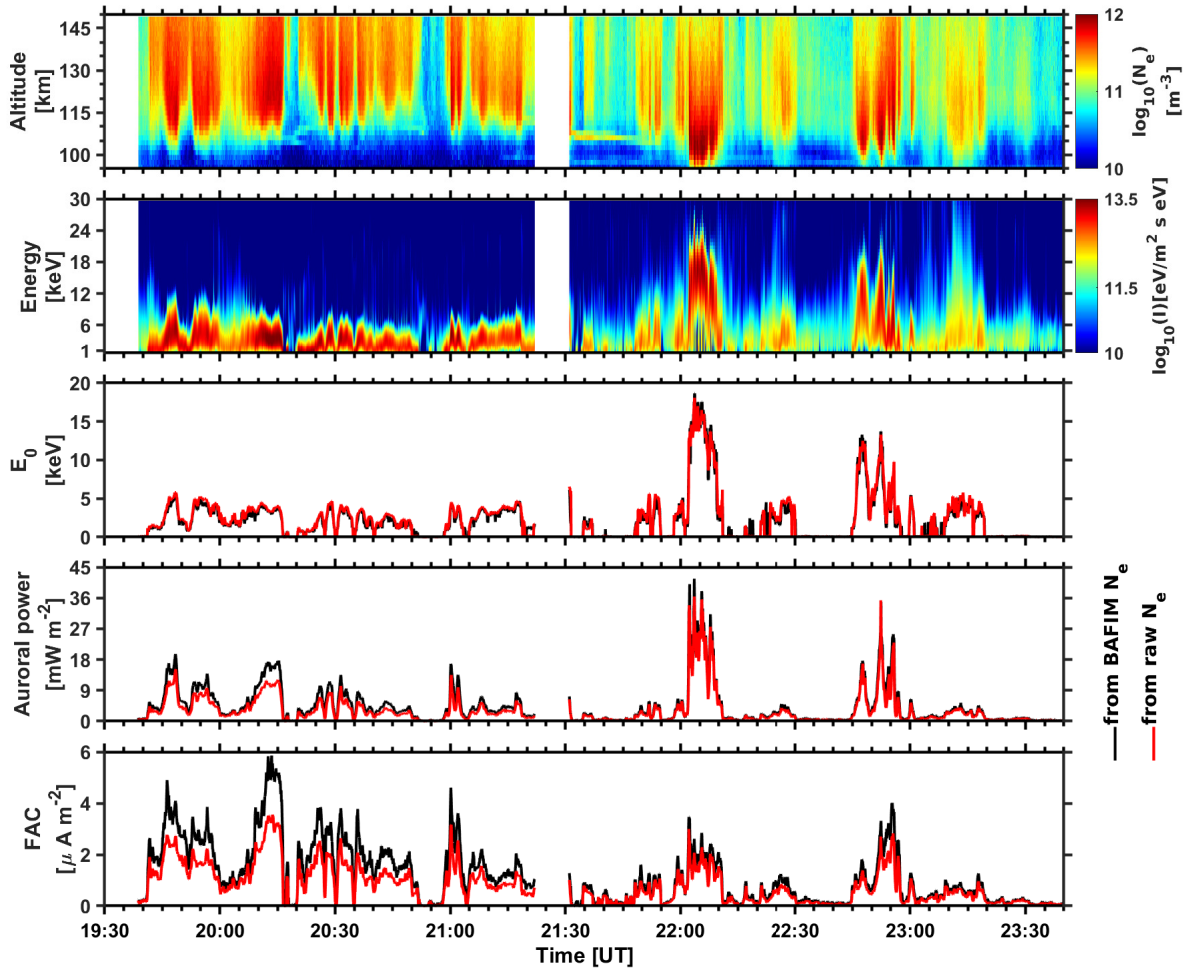

Figure 6. ELSPEC fit results during the whole event. Panels from top to bottom: BAFIM-fitted N_e, differential energy flux, peak energies, auroral powers, and FAC. In panels 3-4, the black and red curves correspond to ELSPEC analysis results using the BAFIM-fitted N_e and raw density N_r, respectively

Several ionization enhancements with different peak altitudes are shown in the electron density plot. Ionization enhancements shown before about 21:30 UT have peak altitudes that lie between 110 and 120 km. Energy distributions of the precipitating electrons that produce these enhancements was peaking between 3 and 5 keV, as shown in the second and third panels. After 21:30 UT, mainly two enhanced ionization periods are shown with lowered peak altitudes in the range between 100 and 106 km. The enhancements are produced by hardening of the precipitating electrons whose energies reach as large as 21 keV, as shown in the second panel of the figure. The largest peak energy and auroral power estimates of the entire event are about 18 keV and 40 mWm^{-2}, respectively, corresponding to the bright and large auroral bulge observed in the post midnight sector during the third substorm, as illustrated in panel I and J of Figure 2. In general, the large ionization enhancements observed before and after 21:30 UT are produced by flux of electrons whose peak energy lies in the range 3 - 5 keV, and 5 - 18 keV, respectively.

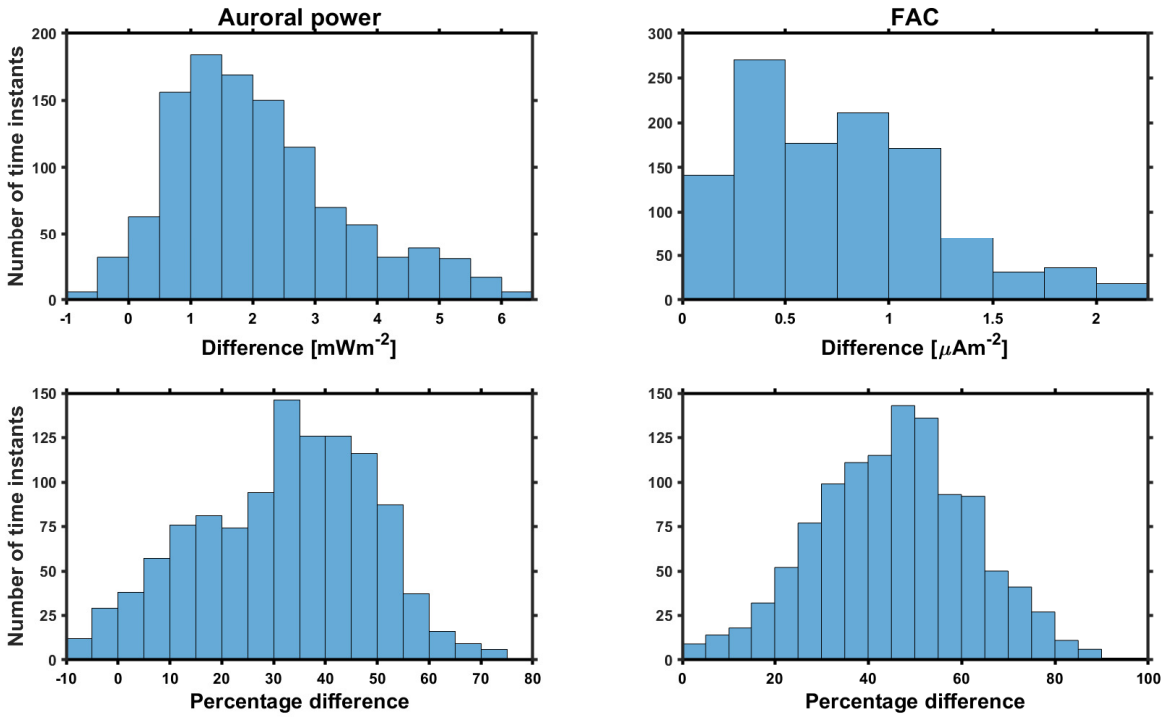

Figure 7. Distribution of the absolute and percentage differences in the auroral power (left panels) and FAC (right panels) estimates.

Inferring the last two panels of the figure, the auroral power and FAC estimates obtained from the BAFIM-fitted N_e significantly exceed their counterparts obtained from the raw density N_r during the first substorm before 21:30 UT. However, during the last two substorm periods after 21:30, the differences become smaller. This is because, before 21:30 UT large flux of lower energy electrons deposit their energy at higher altitudes and heat the electron gas above the ion temperature. Whereas for those periods after 21:30 UT, the electrons become sufficiently energetic and cause enhanced ionization below 115 km altitude, where collisions balance the ion and electron temperatures. Electron temperature was sometimes higher than ion temperature at high altitudes ($>$ 120 km) after 21:30 UT, but this has a relatively small effect on the derivation of auroral power and FAC because peaks of the electron density altitude profiles were at lower altitudes.

Figure 7 presents distribution of the actual and percentage difference between the auroral powers (left panel) and FAC (right panel) calculated from N_e and N_r data of the whole time interval (4 hour). The differences are calculated only for time instants during which the auroral power calculated from N_r is greater than 3 mWm^{-2}. The histograms show that the differences between the auroral power estimates peak in the range 0.5 - 2.5 mWm^{-2} (30 - 45 %). For the FAC estimates, the peak difference is in the range 0.25 - 0.5 $\mu\mathrm{Am}^{-2}$ (45 - 55 %). The largest differences between the auroral power and FAC estimates are about 75 and 90%, respectively. In general, the histograms show that the auroral power and FAC calculated from N_e typically exceed those from N_r, but most of the times the difference is smaller than those extreme cases discussed in Subsection 4.4.

5 Comparison to optical observations

5.1 Auroral power from radar and blue molecular band emission intensity

We validate our radar analysis results by means of comparing radar observations of auroral power with simultaneous, co-located observation of the blue 427.8 nm emission intensity, utilizing their proportionality relationship. The emission intensity data used in this study is in arbitrary pixel count units without being corrected for dark current leakage in the detectors (Nel, 2019), possible contributions from night time air-glow emission, and atmospheric scattering of light from nearby sources. We subtract the background and scale the emission intensities to the same units with the radar data by means of a linear least-square fit between the auroral power and the blue line emission intensity. The emission intensity is the median of pixel intensities inside the radar beam. Equation 3 and Figure 8 show results of the linear fit between the blue line emission data and auroral power estimates calculated from BAFIM-fitted N_e.

$$P = 0.0042 I_{4278} - 3.8333, \tag{3}$$

where P is in mWm^{-2} and the constant term is attributed to the background data sources in the optical data. Figure 8 demonstrates a very good linear relationship between the 427.8 nm emission intensity and the total energy flux of the precipitating electrons. For this particular event, we calculated a cross-correlation coefficient value of 0.96 between the auroral power and the 427.8 nm emission intensity.

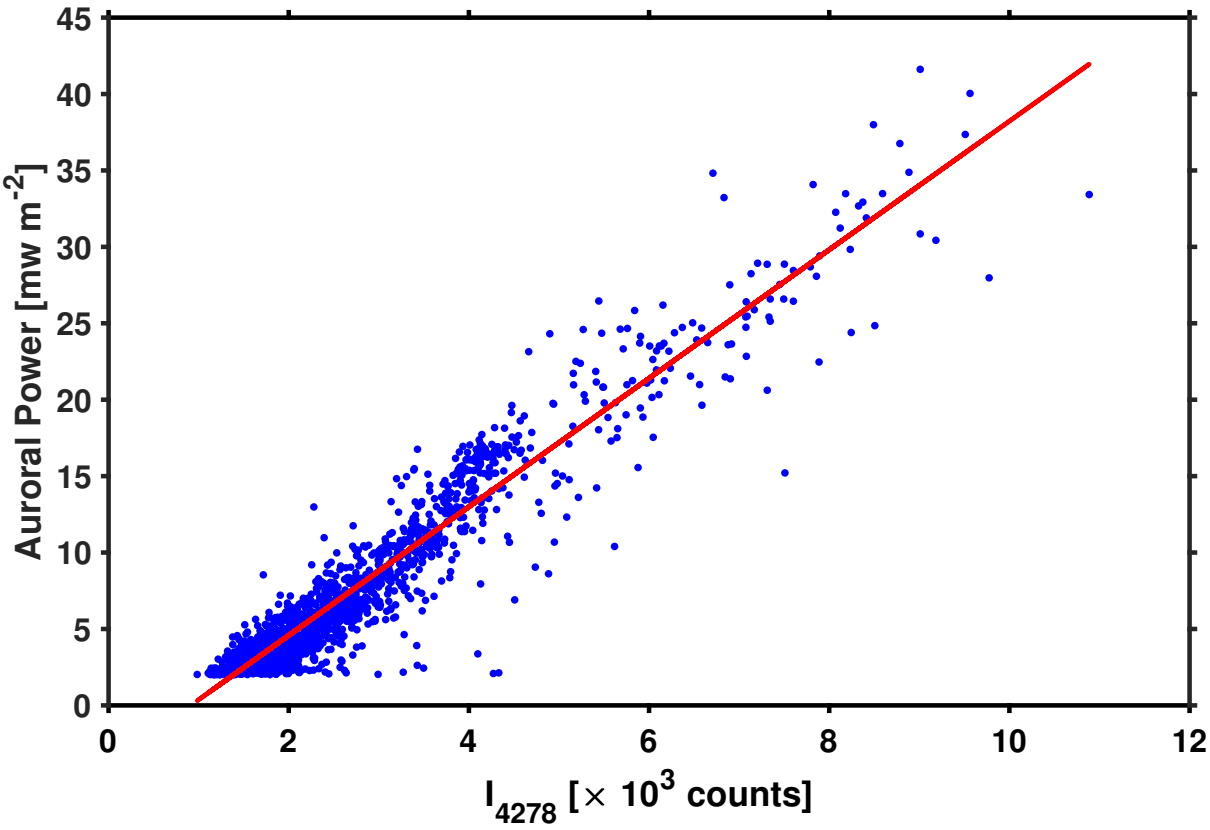

Figure 8. Fitting the blue line emission data to the auroral power calculated by ELSPEC using the BAFIM fitted electron density.

Comparison between the temporal variations of the scaled 427.8 nm emission intensity and the auroral power is shown in the top panel of Figure 9. As shown in the figure, both large scale and small scale variations of the 427.8 nm emission intensity match very well with variations in auroral power calculated from radar data. Furthermore, sharp temporal gradients in the emission intensity are captured precisely by the auroral power calculated from the radar data using the BAFIM-fitted electron density.

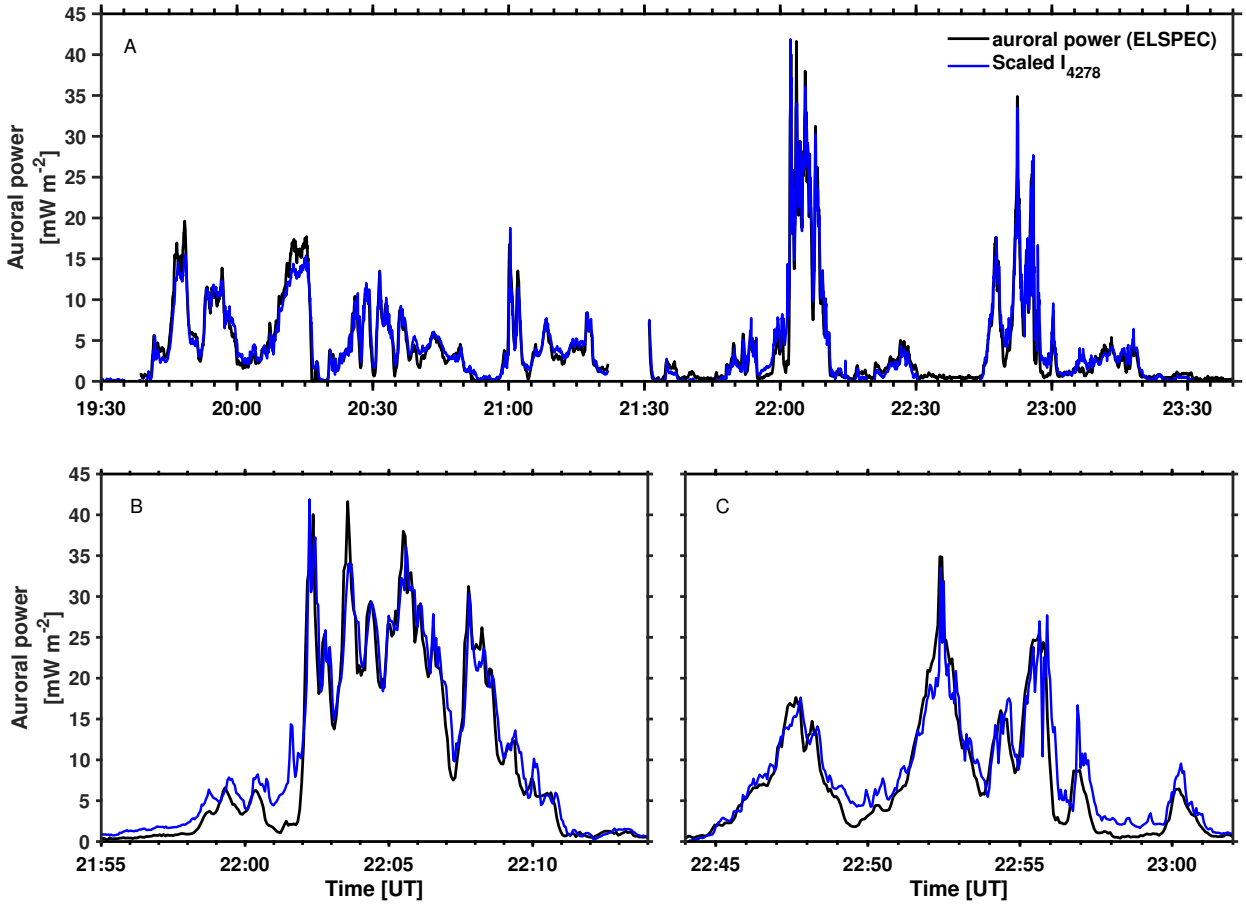

Figure 9. Panel A: Comparing the temporal variations of the auroral power (black) and the scaled emission intensity (blue). Panels B and C: selected periods from panel A.

However, the scaled emission intensity is consistently smaller than the auroral power calculated from the radar data in the time intervals 19:46 − 19:48 UT, and 20:11 − 20:15 UT, during which the flux of about 1 keV electrons was large. Previous studies have shown that the prompt emission rate of blue photons per unit deposited energy decreases with altitude and characteristic energy of the depositing electrons (Rees & Luckey, 1974; Partamies et al., 2004). As a result, our scaled 427.8 nm emission intensities might be underestimates of the auroral power during these time intervals. Another potential cause of the discrepancy is overestimation of the auroral power by ELSPEC due to ion composition variations. The effect of ion composition variations was studied by Virtanen et al. (2018), who found that the Sodankylä Ion and Neutral Chemistry (SIC) model (Turunen et al., 2016) predicts enhanced and rapidly varying O_2^+ to NO^+ ion ratios during electron precipitation, and ELSPEC analysis with O_2^+ to NO^+ ion ratio taken from the International Reference Ionosphere (Bilitza et al., 2017) produced up to 20% larger

auroral powers than the corresponding analysis using SIC ion compositions in an event study.

5.2 Effect of narrow auroral structures on ELSPEC analysis

There are also few time instants when the scaled emission intensity is clearly larger than the auroral power calculated from radar data. For better visualization, selected parts of the comparison graph which contain these time instants are shown separately in panels B and C of Figure 9. Centered at each time instant, narrow FoV auroral images from three subsequent 3 s exposure time are shown in Figure 10.

The first one occurs between 22:01:35 UT and 22:01:41 UT (panel B of Figure 9) when a thin auroral structure with rapidly varying intensity is within the radar beam, as shown in the top panels of Figure 10. The images indicate that the radar beam is not filled uniformly by the arc before and after 22:01:38 UT. In addition, a satellite crossed the radar beam at 22:01:41, and light reflected from the satellite contributes to the observed emission intensity. The satellite is marked with blue arrows the Figure. Panel C of Figure 9 shows the next significant discrepancy at around 22:56:53 UT, when the equatorward edge of an east west elongated arc enters the radar beam and returns back within a time scale shorter than the radar integration time, as shown in the bottom panels of Figure 10.

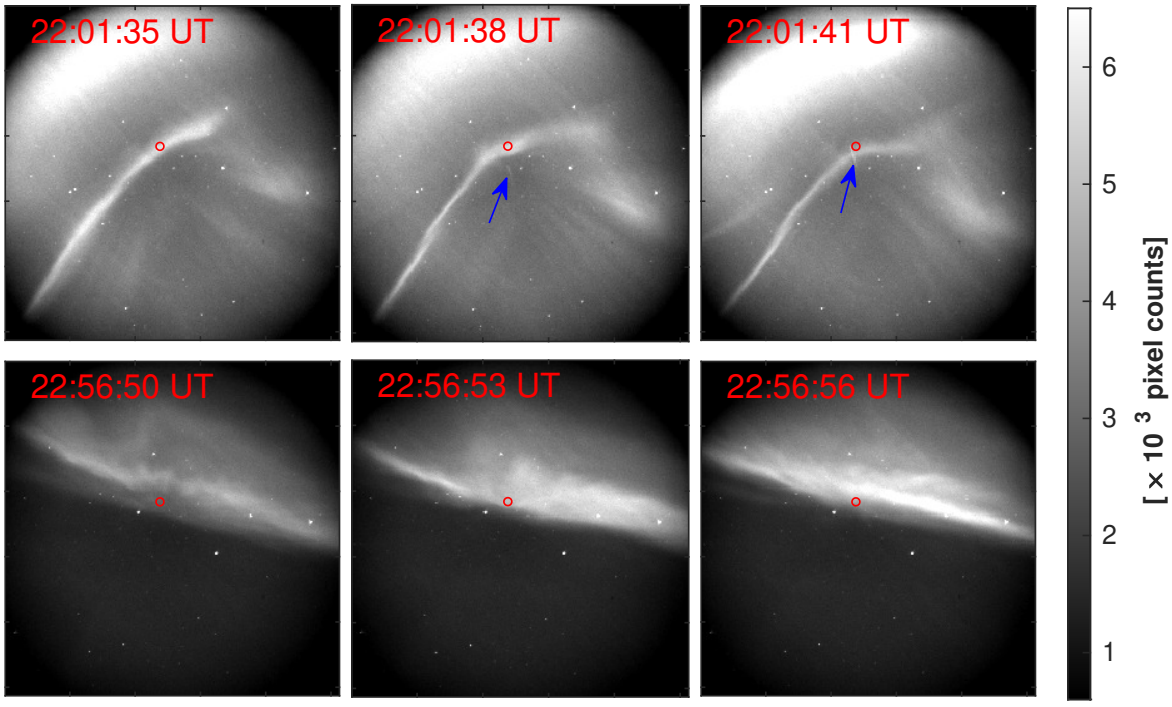

Figure 10. Narrow FoV auroral images at the given instants of time. The red circle represent the radar beam and the arrows indicate to a passing satellite.

The small scale structures and rapid variations are a probable reason for the differences in these cases. The electron densities observed with the radar are averages of electron density over the observation volume and integration time, while the optical ob-

servations are proportional to the ion production rate averaged over the radar beam and exposure time. Our radar analysis then assumes that electron density is uniform within the radar observing volume and finds a constant flux that leads to best fit between modeled and observed electron density profiles. Violating the assumptions of uniform density within the observation volume and constant flux during the radar integration time will readily lead to underestimation of the total flux. We thus have a reason to believe that the optical observations are closer to the true mean auroral power within the radar beam in these cases.

6 Discussion and Summary

This study demonstrates for the first time the applicability of a novel combination of two analysis methods (BAFIM and ELSPEC) for estimation of precipitating electron energy spectra, auroral power, and upward FAC from incoherent scatter radar measurements. The unique advantages of this combined analysis is utilization of the true electron density, instead of the raw electron density, with high time (4 s) and range (1.8 km) resolutions as input for the ELSPEC analysis. The BAFIM-ELSPEC analysis method is applied to an auroral event containing three small substorms that occur in the pre-midnight and post-midnight sectors on 9 March 2016. Below we make a short summary and discussion of the main results of this study.

The four-parameter fits of N_e, T_e, T_i, and V_i to the E region EISCAT UHF ISR data were performed with 4 s / 1.8 km resolutions by using the Bayesian Filtering Module (BAFIM) (Virtanen et al., 2021). We find that N_r is systematically smaller than N_e in the E region when electron precipitation heats the electron gas above the ion temperature. The effect is largest at the top of the E region, where N_e is up to 50 % larger than N_r above 130 km altitude, but significant differences are also observed down to 115 km.

When the true N_e is used in electron energy spectrum fits with ELSPEC (Virtanen et al., 2018), wider energy spectra and larger total fluxes are produced than in the corresponding analysis with N_r as input. Larger number fluxes are produced at the low energy end of the spectra in particular. Auroral power (total energy flux) integrated from the fitted energy spectra are up to 75 % larger than the estimates calculated with N_r as input. However, the distribution of the difference peaks at lower values between 30 - 45 %. Similarly, using the true N_e also yields up to 90 % larger upward FAC estimates than using the raw electron density N_r as input for ELSPEC. However, the distribution of the difference between the FAC estimates during the entire event peaks at smaller values, between 45 - 55 %.

Significant differences between the auroral power estimates are observed during the expansion phase of the first substorm which occurred in the pre-midnight sector in connection to flux of precipitating electrons with peak energies between 3 and 5 keV. The differences become insignificant when the precipitating electrons are sufficiently energetic to produce ionization at lower altitudes, in this study below 115 km. This happens, in this study, corresponding to the post-midnight auroral activities during the second and third substorm periods. The auroral power estimates corresponding to observed ionization enhancements during the night of 9 March 2016 were in the range of 3 - 40 mWm^{-2}. These values are in accordance with several other previous studies (Stenbaek-Nielsen et al., 1998; Dahlgren et al., 2011; Kaeppler et al., 2015). The largest auroral power of the night, 40 mWm^{-2}, was associated with a bright auroral bulge observed in the post-midnight sector as a result of precipitating electrons with peak energies as large as 18 keV.

Finally, the auroral powers calculated using the BAFIM-ELSPEC analysis combination were compared to column intensities of the optical 427.8 nm emission to validate the estimates. A linear correlation between the two were found, and the temporal evolution showed an excellent match. A few significant discrepancies during short time

periods were found, but those were shown to correspond to situations when auroral structures narrower than the radar beam move across the beam, or when the electron energy spectrum changes considerably during a radar integration.

Acknowledgments

We acknowledge the EISCAT Association for the incoherent scatter radar data used in this study. EISCAT is an international association supported by research organizations in China (CRIRP), Finland (SA), Japan (NIPR and STEL), Norway (NFR), Sweden (VR), and the United Kingdom (NERC). EISCAT data are available for download from the EISCAT web page (http://www.eiscat.se). We thank T. Raita, Sodankylä Geophysical Observatory, Finland, for the Kilpisjärvi Pulsation magnetometer data. This work is supported by the Academy of Finland (301542) and the Kvantum institute of the University of Oulu.

References

Aikio, A. T., Lakkala, T., Kozlovsky, A., & Williams, P. J. S. (2002). Electric fields and currents of stable drifting auroral arcs in the evening sector. *Journal of Geophysical Research: Space Physics*, *107*(A12), SIA 3-1-SIA 3-14. doi: https://doi.org/10.1029/2001JA009172

Baron, M. J. (1977). The chatanika radar system. In A. Brekke (Ed.), *Radar probing of the auroral plasma* (p. 103-141). Tromsø, Norway: Universitetsforlaget.

Bilitza, D., Altadill, D., Truhlik, V., Shubin, V., Galkin, I., Reinisch, B., & Huang, X. (2017). International Reference Ionosphere 2016: From ionospheric climate to real-time weather predictions. *Space Weather*, *15*(2), 418-429. doi: 10.1002/2016SW001593

Brekke, A., Hall, C., & Hansen, T. L. (1989, June). Auroral ionospheric conductances during disturbed conditions. *Annales Geophysicae*, *7*, 269-280.

Burns, C., Howarth, W., & Hargreaves, J. (1990). High-resolution incoherent scatter radar measurements during electron precipitation events. *Journal of Atmospheric and Terrestrial Physics*, *52*(3), 205 - 218. doi: https://doi.org/10.1016/0021-9169(90)90124-6

Carlson, C. W., Pfaff, R. F., & Watzin, J. G. (1998). The Fast auroral snapshot (FAST) mission. *Geophysical Research Letters*, *25*(12), 2013-2016. doi: https://doi.org/10.1029/98GL01592

Dahlgren, H., Gustavsson, B., Lanchester, B. S., Ivchenko, N., Brändström, U., Whiter, D. K., ... Marklund, G. (2011). Energy and flux variations across thin auroral arcs. *Annales Geophysicae*, *29*(10), 1699–1712. doi: https://doi.org/10.5194/angeo-29-1699-2011

Dombeck, J., Cattell, C., Prasad, N., Meeker, E., Hanson, E., & McFadden, J. (2018). Identification of auroral electron precipitation mechanism combinations and their relationships to net downgoing energy and number flux. *Journal of Geophysical Research: Space Physics*, *123*(12), 10,064-10,089. doi: https://doi.org/10.1029/2018JA025749

Fang, X., Randall, C. E., Lummerzheim, D., Wang, W., Lu, G., Solomon, S. C., & Frahm, R. A. (2010). Parameterization of monoenergetic electron impact ionization. *Geophysical Research Letters*, *37*(22). doi: https://doi.org/10.1029/2010GL045406

Fujii, R., Nozawa, S., Sato, M., Matuura, N., Ono, T., Brekke, A., ... Hansen, T. L. (1995). Comparison between electron spectra calculated from EISCAT electron density profiles and those observed by the DMSP satellites. *Journal of geomagnetism and geoelectricity*, *47*(8), 771-782. doi: https://doi.org/10.5636/jgg.47.771

Hargreaves, J., & Devlin, T. (1990). Morning sector electron precipitation events

observed by incoherent scatter radar. *Journal of Atmospheric and Terrestrial Physics*, *52*(3), 193 - 203. doi: https://doi.org/10.1016/0021-9169(90)90123-5

Holt, J. M., Rhoda, D. A., Tetenbaum, D., & van Eyken, A. P. (1992, May-June). Optimal analysis of incoherent scatter radar data. *Radio Sci.*, *27*(3), 435-447. doi: https://doi.org/10.1029/91RS02922

Hsu, T.-S., & McPherron, R. L. (2012). A statistical analysis of substorm associated tail activity. *Advances in Space Research*, *50*(10), 1317-1343. doi: https://doi.org/10.1016/j.asr.2012.06.034

Hysell, D. L., Rodrigues, F. S., Chau, J. L., & Huba, J. D. (2008). Full profile incoherent scatter analysis at Jicamarca. *Ann. Geophys.*, *26*, 59-75. doi: 10.5194/angeo-26-59-2008

Kaeppler, S. R., Hampton, D. L., Nicolls, M. J., Strømme, A., Solomon, S. C., Hecht, J. H., & Conde, M. G. (2015). An investigation comparing ground-based techniques that quantify auroral electron flux and conductance. *Journal of Geophysical Research: Space Physics*, *120*(10), 9038-9056. doi: https://doi.org/10.1002/2015JA021396

Kallio, E. I., Pulkkinen, T. I., Koskinen, H. E. J., Viljanen, A., Slavin, J. A., & Ogilvie, K. (2000). Loading-unloading processes in the nightside ionosphere. *Geophysical Research Letters*, *27*(11), 1627-1630. doi: https://doi.org/10.1029/1999GL003694

Kirkwood, S. (1988). *SPECTRUM: A computer algorithm to derive the flux-energy spectrum of precipitating particles from EISCAT electron density profiles.*

Kirkwood, S., & Eliasson, L. (1990). Energetic particle precipitation in the substorm growth phase measured by EISCAT and Viking. *Journal of Geophysical Research: Space Physics*, *95*(A5), 6025-6037. doi: https://doi.org/10.1029/JA095iA05p06025

Kosch, M. J., Honary, F., del Pozo, C. F., Marple, S. R., & Hagfors, T. (2001). High-resolution maps of the characteristic energy of precipitating auroral particles. *Journal of Geophysical Research: Space Physics*, *106*(A12), 28925-28937. doi: https://doi.org/10.1029/2001JA900107

Lanchester, B. S., Kaila, K., & McCrea, I. W. (1996). Relationship between large horizontal electric fields and auroral arc elements. *Journal of Geophysical Research: Space Physics*, *101*(A3), 5075-5084. doi: https://doi.org/10.1029/95JA02055

Lanchester, B. S., Palmer, J. R., Rees, M. H., Lummerzheim, D., Kaila, K., & Turunen, T. (1994). Energy flux and characteristic energy of an elemental auroral structure. *Geophysical Research Letters*, *21*(25), 2789-2792. doi: https://doi.org/10.1029/94GL01764

Lanchester, B. S., Rees, M. H., Lummerzheim, D., Otto, A., Frey, H. U., & Kaila, K. U. (1997). Large fluxes of auroral electrons in filaments of 100 m width. *Journal of Geophysical Research: Space Physics*, *102*(A5), 9741-9748. doi: https://doi.org/10.1029/97JA00231

Lehtinen, M. S., & Häggström, I. (1987). A new modulation principle for incoherent scatter measurements. *Radio Sci.*, *22*, 625-634. doi: https://doi.org/10.1029/RS022i004p00625

Lehtinen, M. S., & Huuskonen, A. (1996). General incoherent scatter analysis and GUISDAP. *Journal of Atmospheric and Terrestrial Physics*, *58*(1), 435 - 452. doi: https://doi.org/10.1016/0021-9169(95)00047-X

Lehtinen, M. S., Huuskonen, A., & Pirttilä, J. (1996, December). First experiences of full-profile analysis with GUISDAP. *Ann. Geophys.*, *14*, 1487-1495. doi: https://doi.org/10.1007/s00585-996-1487-3

McPherron, R. L. (2005, Sep 01). Magnetic pulsations: Their sources and relation to solar wind and geomagnetic activity. *Surveys in Geophysics*, *26*(5), 545-592. doi: 10.1007/s10712-005-1758-7

Mishin, V. V., Tsegmed, B., Klibanova, Y. Y., & Kurikalova, M. A. (2020). Burst geomagnetic pulsations as indicators of substorm expansion onsets during storms. *Journal of Geophysical Research: Space Physics*, *125*(10), e2020JA028521. doi: https://doi.org/10.1029/2020JA028521

Nel, A. E. (2019). *Novel radar and optical observations of black auroras in the upper atmosphere* (Doctoral dissertation, North-West University). `https://repository.nwu.ac.za/handle/10394/35266`.

Nel, A. E., Kosch, M. J., Whiter, D., Gustavsson, B., & Aslaksen, T. (2021, Jan 19). A new auroral phenomenon, the anti-black aurora. *Scientific Reports*, *11*(1), 1829. doi: https://doi.org/10.1038/s41598-021-81363-9

Newell, T., Sotirelis, T., & Wing, S. (2009). Diffuse, monoenergetic, and broadband aurora: The global precipitation budget. *Journal of Geophysical Research: Space Physics*, *114*(A9). doi: https://doi.org/10.1029/2009JA014326

Ogawa, Y., Tanaka, Y., Kadokura, A., Hosokawa, K., Ebihara, Y., Motoba, T., ... Fujii, R. (2020). Development of low-cost multi-wavelength imager system for studies of aurora and airglow. *Polar Science*, *23*, 100501. doi: https://doi.org/10.1016/j.polar.2019.100501

Olson, J. V. (1999). Pi2 pulsations and substorm onsets: A review. *Journal of Geophysical Research: Space Physics*, *104*(A8), 17499-17520. doi: https://doi.org/10.1029/1999JA900086

Omholt, A. (1971). The electron aurora: Main characteristics and luminosity. In *Physics and chemistry in space* (p. 24–46). Springer Berlin Heidelberg. doi: 10.1007/978-3-642-46269-6_2

Osepian, A., & Kirkwood, S. (1996). High-energy electron fluxes derived from EISCAT electron density profiles. *Journal of Atmospheric and Terrestrial Physics*, *58*(1), 479 - 487. doi: https://doi.org/10.1016/0021-9169(95)00050-X

Partamies, N., Janhunen, P., Kauristie, K., Mäkinen, S., & Sergienko, T. (2004). Testing an inversion method for estimating electron energy fluxes from all-sky camera images. *Annales Geophysicae*, *22*(6), 1961–1971. doi: https://doi.org/10.5194/angeo-22-1961-2004

Rees, M. H. (1963). Auroral ionization and excitation by incident energetic electrons. *Planetary and Space Science*, *11*(10), 1209 - 1218. doi: https://doi.org/10.1016/0032-0633(63)90252-6

Rees, M. H., & Luckey, D. (1974). Auroral electron energy derived from ratio of spectroscopic emissions 1. Model computations. *Journal of Geophysical Research (1896-1977)*, *79*(34), 5181-5186. doi: https://doi.org/10.1029/JA079i034p05181

Saito, T. (1969, December). Geomagnetic Pulsations. *Space Science Review*, *10*(3), 319–412. doi: https://doi.org/10.1007/BF00203620

Sakurai, T., & Saito, T. (1976). Magnetic pulsation pi2 and substorm onset. *Planetary and Space Science*, *24*(6), 573 - 575. doi: https://doi.org/10.1016/0032-0633(76)90135-5

Semeter, J., & Kamalabadi, F. (2005). Determination of primary electron spectra from incoherent scatter radar measurements of the auroral E region. *Radio Science*, *40*(2). doi: https://doi.org/10.1029/2004RS003042

Sheehan, C. H., & St.-Maurice, J.-P. (2004). Dissociative recombination of N_2^+, O_2^+, and NO^+: Rate coefficients for ground state and vibrationally excited ions. *Journal of Geophysical Research: Space Physics*, *109*(A3). doi: https://doi.org/10.1029/2003JA010132

Simon Wedlund, C., Lamy, H., Gustavsson, B., Sergienko, T., & Brändström, U. (2013). Estimating energy spectra of electron precipitation above auroral arcs from ground-based observations with radar and optics. *Journal of Geophysical Research: Space Physics*, *118*(6), 3672-3691. doi: https://doi.org/10.1002/jgra.50347

Stenbaek-Nielsen, H. C., Hallinan, T. J., Osborne, D. L., Kimball, J., Chaston, C.,

McFadden, J., ... Carlson, C. W. (1998). Aircraft observations conjugate to FAST: Auroral are thicknesses. *Geophysical Research Letters*, *25*(12), 2073-2076. doi: https://doi.org/10.1029/98GL01058

Strickland, D. J., Hecht, J. H., Christensen, A. B., & Kelly, J. (1994). Relationship between energy flux Q and mean energy E of auroral electron spectra based on radar data from the 1987 CEDAR campaign at Sondre Stromfjord, Greenland. *Journal of Geophysical Research: Space Physics*, *99*(A10), 19467-19473. doi: https://doi.org/10.1029/94JA01901

Strickland, D. J., Meier, R. R., Hecht, J. H., & Christensen, A. B. (1989). Deducing composition and incident electron spectra from ground-based auroral optical measurements: Theory and model results. *Journal of Geophysical Research*, *94*(A10), 13527. doi: https://doi.org/10.1029/ja094ia10p13527

Tanskanen, E. I. (2009). A comprehensive high-throughput analysis of substorms observed by IMAGE magnetometer network: Years 1993–2003 examined. *Journal of Geophysical Research: Space Physics*, *114*(A5). doi: https://doi.org/10.1029/2008JA013682

Turunen, E., Kero, A., Verronen, P. T., Miyoshi, Y., Oyama, S.-I., & Saito, S. (2016). Mesospheric ozone destruction by high-energy electron precipitation assciated with pulsating aurora. *J. Geophys. Res. Atmos.*, *121*, 11852-11861. doi: 10.1002/2016JD025015

Virtanen, I. I., Gustavsson, B., Aikio, A., Kero, A., Asamura, K., & Ogawa, Y. (2018). Electron energy spectrum and auroral power estimation from incoherent scatter radar measurements. *Journal of Geophysical Research: Space Physics*, *123*(8), 6865-6887. doi: 10.1029/2018JA025636

Virtanen, I. I., Tesfaw, H. W., Roininen, L., Lasanen, S., & Aikio, A. (2021). Bayesian filtering in incoherent scatter plasma parameter fits. *Journal of Geophysical Research: Space Physics*, *126*(3), e2020JA028700. doi: https://doi.org/10.1029/2020JA028700

Vondrak, R. R., & Baron, M. J. (1977). A method of obtaining the energy distribution of auroral electrons from incoherent scatter radar measurements. In A. Brekke (Ed.), *Radar probing of the auroral plasma* (p. 315-330). Tromsø, Norway: Universitetsforlaget.

Wickwar, V. B., Lathuillere, C., Kofman, W., & Lejeune, G. (1981). Elevated electron temperatures in the auroral E layer measured with the chatanika radar. *Journal of Geophysical Research: Space Physics*, *86*(A6), 4721-4730. doi: https://doi.org/10.1029/JA086iA06p04721